

Resolving the Ambiguity of Complete-to-Partial Point Cloud Registration for Image-Guided Liver Surgery with Patches-to-Partial Matching

Zixin Yang, Jon S. Heiselman, Cheng Han, Kelly Merrell, Richard Simon, Cristian. A. Linte.

Abstract—In image-guided liver surgery, the initial rigid alignment between preoperative and intraoperative data, often represented as point clouds, is crucial for providing sub-surface information from preoperative CT/MRI images to the surgeon during the procedure. Currently, this alignment is typically performed using semi-automatic methods, which, while effective to some extent, are prone to errors that demand manual correction. Point cloud correspondence-based registration methods are promising to serve as a fully automatic solution. However, they may struggle in scenarios with limited intraoperative surface visibility, a common challenge in liver surgery, particularly in laparoscopic procedures, which we refer to as complete-to-partial ambiguity. We first illustrate this ambiguity by evaluating the performance of state-of-the-art learning-based point cloud registration methods on our carefully constructed *in silico* and *in vitro* datasets. Then, we propose a patches-to-partial matching strategy as a plug-and-play module to resolve the ambiguity, which can be seamlessly integrated into learning-based registration methods without disrupting their end-to-end structure. It has proven effective and efficient in improving registration performance for cases with limited intraoperative visibility. The constructed benchmark and the proposed module establish a solid foundation for advancing applications of point cloud correspondence-based registration methods in image-guided liver surgery. Code and datasets will be released.

Index Terms—Image-guided liver surgery, point cloud matching, pre- to intraoperative rigid registration.

I. INTRODUCTION

IN liver surgery, preoperative imaging techniques such as Computed Tomography (CT) and Magnetic Resonance Imaging (MRI) provide detailed information about critical anatomical structures, such as blood vessels and tumors. However, this information is not usually available during surgery due to the large footprint of the equipment, its immobility, and its prohibitively high cost. Consequently, intraoperative imaging is most commonly limited to lower resolution or partial information covering only a portion of the visible organ

This work was supported by the National Institutes of Health - National Institute of General Medical Sciences under Award No. R35GM128877 and the National Science Foundation - Office of Advanced Cyber-infrastructure under Award No.1808530 and the Division of Chemical, Bioengineering and Transport Systems under Award No. 2245152.

Zixin Yang, Richard Simon, Kelly Merrell, and Cristian. A. Linte are with the Center for Imaging Science and Department of Biomedical Engineering, Rochester Institute of Technology, Rochester, USA.

Jon S. Heiselman is with the Department of Biomedical Engineering, Vanderbilt University, USA.

Cheng Han is with the School of Science and Engineering, University of Missouri – Kansas City, USA.

Email: Zixin Yang, yy8898@rit.edu.

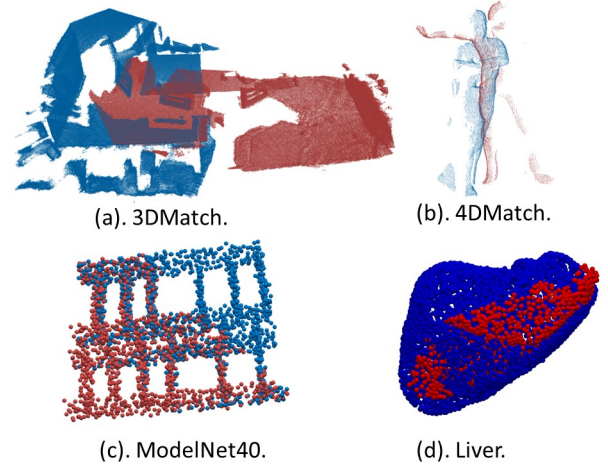


Fig. 1. Comparison of widely used public point registration datasets in computer vision (3DMatch, 4DMatch, ModelNet40) and our liver registration dataset. In each example, the source point clouds (blue) are aligned with the target point clouds (red). 3DMatch, 4DMatch, and ModelNet40 focus on partial-to-partial cases. The liver registration dataset is distinct from these datasets, designed under the complete-to-partial scenarios.

from modalities including intraoperative ultrasound [1], [2], cone-beam CT (CBCT) [3], [4], and optical cameras [5]–[8]. To inform the surgeon of subsurface information from preoperative CT/MRI during surgery, a registration process is involved to compute the transformation between the preoperative and intraoperative data in image-guided surgery (IGS) systems, which is generally divided into two steps.

Step 1 is an initial rigid registration to resolve the problem that preoperative and intraoperative data are acquired in different coordinate systems. However, current IGS systems often perform this alignment semi-automatically [9], bringing considerable time consumption and susceptibility to errors [10].

Step 2 involves non-rigid registration methods to estimate tissue deformations, which depend on an accurate initial rigid registration.

Registration methods that adapt to available intraoperative information can be categorized into intensity-based, 3D-to-2D, and 3D-to-3D methods. This paper addresses the initial rigid registration problem in a 3D-to-3D context, where both the preoperative and intraoperative data are represented as 3D point clouds. The preoperative point cloud is often derived from CT or MRI scans, while the intraoperative point cloud

is often captured using 3D sensors or reconstructed from endoscopic video images via 3D reconstruction. For clarity, we refer to the point cloud representing the entire liver from the preoperative surface as the **source point cloud** and the partial intraoperative point cloud as the **target point cloud**.

Learning-based point cloud registration methods, particularly correspondence-based approaches, have shown promising results [11]–[14] to solve the limitations of semi-automatic methods. However, applying these methods, designed for natural datasets, to liver surgery is challenging due to two reasons:

I. Insufficient intraoperative-oriented design. Most learning-based point cloud registration methods are designed for partial-to-partial cases, where point cloud pairs are captured from different view angles and have roughly similar scales. These pairs typically come from RGB-D cameras [12] (Fig. 1 (a)), simulated depth maps from animated sequences [13] (Fig. 1 (b)), or synthetic objects [15], [16] (Fig. 1 (c)). Those pairs often feature prominent structures, such as edges and corners from natural scenes. In liver surgery, particularly in laparoscopic liver surgery, on the other hand, only a partial liver surface is visible intraoperatively: typically around 20–30% of the surface [17] is visible. The partially observable liver surface is matched against the complete liver surface segmented from the preoperative images. Since the viewpoint can change during the procedure, i.e., there is no strong prior knowledge as to what sub-region of the preoperative liver surface should match the intraoperative point cloud match.

As a further challenge, the smooth surface of the liver lacks strong visual key points that could assist with matching partial point clouds and complicates current approaches to accurately align the visible intraoperative portion with the complete preoperative liver model (i.e., see Fig. 1 (d), where the target point cloud has a limited visible surface area). Besides the confusion associated with matching to the top or bottom of the liver, there is also ambiguity when registering a small point cloud to regions to regions adjacent to the liver dome.

As such, we argue that current learning-based point cloud registration methods are insufficient to handle the complete-to-partial ambiguity that frequently arises in LLS.

II. Substantial data requirements. The success of learning-based point cloud registration methods is heavily based on scaled-up datasets. However, this is particularly challenging for liver surgery as collecting extensive *in vivo* or *in vitro* datasets is expensive, complex, and time-consuming. A common practice to capture the preoperative and intraoperative configurations of the liver is to embed fiducial markers. However, this process may cause damage to tissues or phantoms. An alternative is to use simulated data for training and then apply the model to real-world *in vivo* or *in vitro* data [18]. While promising, there is currently a scarcity of large, publicly accessible simulated datasets, and the availability of real-world testing datasets remains severely constraining.

A. Contribution

To address the first challenge, we propose a novel, learnable-parameter-free approach that integrates seamlessly

with correspondence-based point cloud registration methods to mitigate complete-to-partial ambiguity (see §III-B). Our approach significantly improves low-visibility performance with negligible computational overhead. The core concept is to transform the complete-to-partial point cloud registration problem into a subdivided matching problem between the partial point cloud and multiple patches extracted from the complete cloud, which we refer to as patches-to-partial (P2P) matching.

In the P2P, we first select the most likely visible points from the source point cloud. Then, we generate several candidate patches of approximately the same size as the target point cloud. Finally, we match the target point cloud to these candidate patches and aggregate a robust, rigid point cloud transformation by selecting the best estimate across candidates. This module only involves feature resampling and rematching, allowing it to be parallelized for fast execution. Additionally, it is fully differentiable, making it suitable for integration into different correspondence-based point cloud and learning-based registration pipelines.

To address the second challenge, we developed a large simulated dataset comprising over 1,000 liver models and 10,000 simulations alongside phantom datasets (see §IV-A), providing valuable resources for benchmarking and future advancing research in the liver registration area.

We experimentally demonstrate that the current state-of-the-art correspondence-based registration methods are not sufficient when dealing with complete-to-partial ambiguity. We then show the effectiveness of our proposed module in dealing with low-visibility cases after seamless plug-and-play integration into two promising methods. Without any adjustment to loss functions, additional learnable modules, outlier rejection methods, etc., our approach significantly improves complete-to-partial registration.

II. RELATED WORK

A. Traditional point cloud registration

Iterative Closest Point (ICP) [19] and its variants are commonly used in semi-automatic registration processes. ICP iteratively finds the closest points between two point clouds and estimates the rigid transformation using singular value decomposition (SVD) [20]. Though intuitive, ICP is sensitive to initial alignment. Globally optimal ICP (GO-ICP) [21] poses an alternative approach by introducing a global search strategy to improve robustness. However, it then becomes computationally expensive and does not always guarantee an optimal solution.

B. Learning-based point cloud registration

Learning-based point cloud registration methods can be broadly categorized into correspondence-based and direct registration approaches. Correspondence-based methods [12], [13] first establish corresponding point pairs between two point clouds, then compute the optimal transformation based on these correspondences. Direct registration methods [22], [23], on the other hand, directly regress the rigid transformation from global features. While these methods show promising

results on synthetic, object-centric point clouds [15], they usually struggle with low overlap ratios, limited transformation ranges, and larger-scale scenes [12], [24]. Currently, the state-of-the-art techniques assessed on publicly available benchmarking datasets [11]–[13] are correspondence-based.

Representative correspondence-based methods, such as 3DMatch [11], Predator [12], and Leopard [13], introduce techniques like Siamese networks, attention modules, and positional encoding to improve point cloud matching. These techniques and their variants have since become standard practice in correspondence-based methods. While most of these methods focus directly on fine-scale correspondences, some, such as those reported in [14], [25], [26], adopt a point-to-node grouping strategy, where coarse-scale matches guide fine-scale correspondences within patches. However, whether this strategy performs well on datasets with complete-to-partial ambiguity remains unclear. Thus, a representative method [26] using the strategy is included in the experiments.

Early correspondence-based methods [11], [12] rely on RANSAC, a widely known robust estimator that iteratively selects subsets of correspondences to find the best transformation. However, RANSAC often suffers from slow convergence [27] and is unsuitable for end-to-end learning schemes. Consequently, recent methods aim to achieve comparable results without relying on RANSAC. For instance, RegTr [24] directly predicts keypoint displacements, while RoITr [26] uses a local-to-global registration approach to eliminate the need for RANSAC.

Overall, correspondence-based methods have a strong foundation in several public benchmarks for natural datasets. Still, they are not designed to handle the complete-to-partial cases encountered in liver surgery.

C. 3D-3D Initial Rigid Registration in Liver Surgery

Automatic correspondence methods using hand-crafted feature descriptors have been explored by Dos Santos *et al.* [28] and Robu *et al.* [29]. However, these methods have limited accuracy and often require additional pruning.

Several learning-based methods [30]–[32] have been proposed for 3D-3D liver registration, yielding promising results. However, these outcomes should be interpreted with caution. For example, the simulation dataset used in [31] assumes one-to-one correspondence, as both the source and target point clouds are derived from the same mesh without post-processing. Consequently, models pre-trained or fine-tuned on these datasets may struggle when applied to real-world data. Furthermore, Guan *et al.* [30] and Zhang *et al.* [32] treat the intraoperative CT surface as the preoperative surface in the porcine dataset [33], resulting in source and target point clouds with no deformation.

In contrast, we carefully post-process our simulations to include soft tissue deformations, eliminate one-to-one correspondences, and remove rigid components from the simulated deformations. We evaluate the selected registration methods on both our simulation and phantom datasets, ensuring a more rigorous and realistic assessment.

III. METHODOLOGY

This section introduces our proposed patches-to-partial strategy as a plug-and-play module that can be seamlessly integrated into current learning-based correspondence registration methods. We begin by presenting the general paradigm of learning-based correspondence registration methods (see §III-A), followed by a detailed module explanation (see §III-B). The overall framework is illustrated in Fig. 2.

A. Preliminaries

Given a source point cloud $\mathbf{S} \in \mathbb{R}^{N \times 3}$ (preoperative) and a target point cloud $\mathbf{T} \in \mathbb{R}^{M \times 3}$ (intraoperative) as inputs, correspondence-based registration methods output their respective point-wise features, $\mathbf{x}^{\mathbf{S}} \in \mathbb{R}^{N \times d}$ and $\mathbf{x}^{\mathbf{T}} \in \mathbb{R}^{M \times d}$, along with the rigid transformation from \mathbf{S} to \mathbf{T} . Here, N and M represent the number of participating points in the source and target point clouds, respectively, and d is the feature dimension. These registration methods generally consist of four key components: *Feature extraction network*, *Matching module*, *Rigid transformation estimation module*, and *Loss functions*.

Feature extraction networks extract point-wise feature descriptors from both the source and target point clouds. These networks typically use a point cloud feature learning backbone, such as PointNet++ [34], KPConv [35], or Point Transformer [36], which usually involves a U-Net-like structure that gradually down-samples the input point clouds to extract features, followed by upsampling to restore the resolution of the original points while preserving the extracted features.

Attention mechanisms, which have emerged as a pivotal component for feature understanding in various domains [12], [13], [26], are frequently incorporated within the feature learning backbone, particularly in the bottleneck, to empower the interaction between local geometric features towards global geometry-aware ones. This interaction can occur either within the same point cloud (self-attention) or across different point clouds (cross-attention), depending on the layer used.

Matching modules then use either Sinkhorn optimal transport algorithm [26], [37] or dual-softmax operation [13], [38] to match the source and target feature descriptors, which output correspondences between source and target point clouds and their confidences.

Rigid transformation estimation modules further utilize the estimated correspondences and confidences from the matching module and calculate the rigid transformation, using the SVD or weighted SVD [19], [39]. If the estimated correspondences contain a large portion of outliers, the weighted SVD tends to predict an inaccurate rigid transformation. In this case, additional outlier rejection methods are involved in sampling inlier correspondence (e.g., RANSAC).

Loss functions consist of one or more types, such as classification-based loss [13] (e.g., cross-entropy with dual-softmax or optimal transport), feature metric-based loss [12], [26] (e.g., circle loss), and displacement-based loss for predicted matches or estimated rigid transformation accuracy in 3D space.

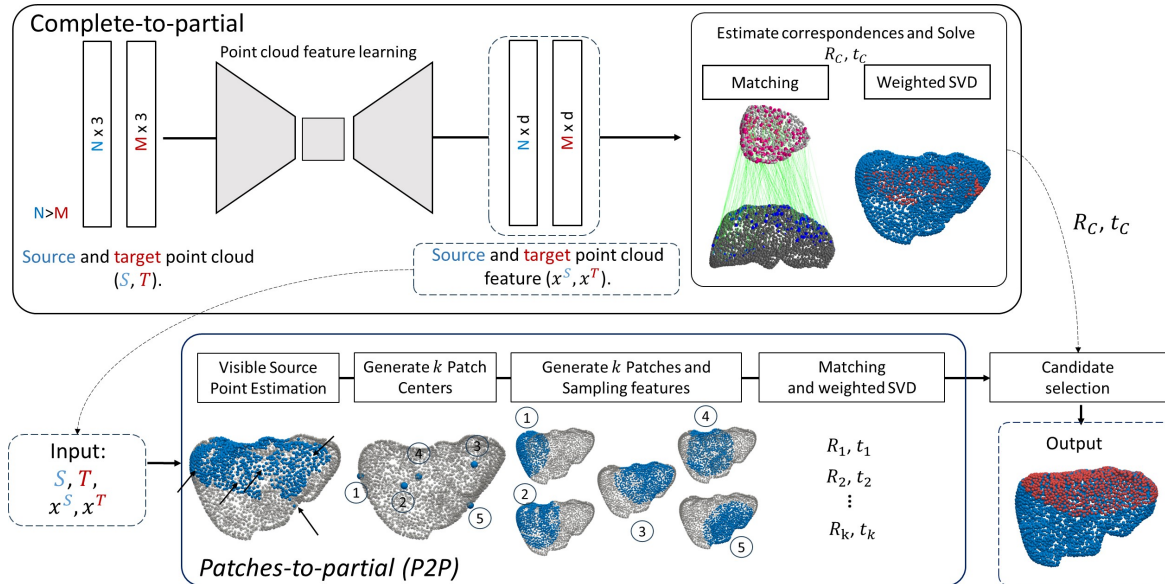


Fig. 2. Illustration of the general paradigm of learning-based correspondence registration methods (top) and our plug-and-play patches-to-partial (P2P) module (bottom). Our proposed module generates candidate patches, samples their point-wise features from a learning-based correspondence registration method, and performs feature matching and rigid transformation estimation for each patch with the target point cloud. Finally, a candidate selection rule determines the optimal rigid transformation. We present the case where the patch number k is set to 5.

B. Transferring complete-to-partial into patches-to-partial matching

The smoothly shaped surface of the liver produces a challenge for point cloud matching wherein the partial target point cloud may incorrectly match well with multiple candidate regions within the source point cloud due to shallow variations in surface curvature. Although correspondence-based registration methods are well-established in several public natural benchmarks, they are not designed to address the complete-to-partial ambiguity inherent in this scenario.

This challenge is similar to a Jigsaw puzzle, where a player tries different candidate spaces to find the correct fit. Inspired by this analogy, we propose converting the complete-to-partial point cloud matching problem into a patches-to-partial (P2P) matching process. By generating several candidate patches from the source point cloud, each roughly the size of the target, and matching them to the target, we can naturally solve the complete-to-partial ambiguity. The questions thus become clear: ❶ *How do we efficiently generate candidate patches from the source point cloud?* ❷ *How do we select the best transformation?*

For consistency in the presentation, we use the point-wise features \mathbf{x}^S and \mathbf{x}^T , along with the estimated transformation $\mathbf{R}_c, \mathbf{t}_c$ from existing correspondence-based registration methods, as our starting point to address these questions and validate this approach.

1) *Visible Source Point Estimation:* In response to ❶, a straightforward approach is to recognize each point from the source point cloud as a patch center and select its nearest neighbors, matching the number of points in the target cloud to generate candidate patches. However, this approach requires impractical computational memory. A more efficient approach would be to first narrow down the candidate points before generating these patches, which this part seeks to present

rigorously.

To narrow down the candidate points, we first design a method to select the top candidates from the source point cloud based on a visibility score, which we define according to a score matrix following [13], [40] as $S = \mathbf{x}^S(\mathbf{x}^T)^T \in \mathbb{R}^{N \times M}$, where S represents the cosine similarity between source and target features. We then convert this score matrix into visibility scores for the source point cloud by summing over the target dimension: $S_{vis} = \sum_{j=1}^M S_{i,j}$. Finally, we select the top M source points with the highest visibility scores to form the visible source point cloud.

2) *Patch Candidate Generation:* The visible source point cloud contains both correct and uncertain points due to complete-to-partial ambiguity. The points are distributed across a region, and it is assumed that matching a patch within this region to the target point cloud facilitates a more precise estimation of rigid transformation compared to utilizing the entire point cloud. Consequently, our next step is to generate a few patches from the region. To do this, we apply farthest point sampling (FPS) [16] to the visible source point cloud, selecting k points to serve as patch nodes.

3) *Patch Sampling and Feature Computation:* The 3D locations and features of candidate patches are then sampled and generated from the nearest neighbors of these patch nodes, with the same number of points as the target point cloud. We denote the features and 3D locations of the k -th source patch as $\mathbf{x}^{S_k} \in \mathbb{R}^{M \times d}$ and $\mathbf{S}_k \in \mathbb{R}^{M \times 3}$, respectively.

4) *Patch-to-Target Matching:* Each patch candidate generated in the previous step is then matched to the target point cloud to establish correspondences via rigid transformation estimation. Taking one patch as an example, we first compute the score matrix $S_k = \mathbf{x}^{S_k}(\mathbf{x}^T)^T \in \mathbb{R}^{N \times M}$, and apply the dual-softmax operation [13], [38], [40]:

$$M_k(i, j) = \text{Softmax}(S_k(i, :)) \cdot \text{Softmax}(S_k(:, j)), \quad (1)$$

where the dual-softmax operation converts S_k into a confidence matrix M_k . Matches are selected from M_k using the mutual nearest neighbor criterion, where a pair of indices (i, j) is chosen if its confidence value $M_k(i, j)$ is the maximum in both $S_k(i, \cdot)$ and $S_k(\cdot, j)$.

Once the correspondence set C_k is obtained, the weighted SVD is applied to compute the rigid transformations \mathbf{R}_k and \mathbf{t}_k . The transformations estimated from each patch are inputs to the next step.

5) *Optimal Candidate Selection*: A candidate selection procedure is needed in our design to select the most likely rigid transformation from the patches, answering ②. One possible solution for candidate selection is to apply the inlier number selection rule used in the point-to-node strategy [25], [26]. This approach selects the best transformation by choosing the one that results in the most inlier matches:

$$\mathbf{R}, \mathbf{t} = \max_{\mathbf{R}_i, \mathbf{t}_i} \sum_{(p_j^S, p_j^T) \in C_{all}} [\|\mathbf{R}_j \cdot p_j^S + \mathbf{t}_j - p_j^T\|_2^2 < \tau], \quad (2)$$

where the Iverson bracket $[\cdot]$ evaluates whether the condition holds, τ is the acceptance radius. C_{all} combines all correspondences from the original output and all C_k from the previous step. p_j^S and p_j^T are 3D points within the correspondences.

The transformations \mathbf{R}_i and \mathbf{t}_i are from the original output and all candidate transformations $\mathbf{R}_k, \mathbf{t}_k$. However, this inlier-based selection favors more feature-matching evaluation metrics (e.g., inlier ratio [12]), while our goal is to select the best rigid transformation. In light of this view, we propose a straightforward selection rule by directly calculating the mean closest point distance between the transformed source point cloud, $\mathbf{R}_i \cdot x^S + \mathbf{t}_i$, and the target point cloud x^T as:

$$\mathbf{R}, \mathbf{t} = \min_{\mathbf{R}_i, \mathbf{t}_i} \sum_{j=1}^M \text{Dist}_{min}(\mathbf{R}_i \cdot x^S + \mathbf{t}_i, x_j^T), \quad (3)$$

where Dist_{min} is the closest point operator that computes the distance from x_j^T to the transformed source point $\mathbf{R}_i \cdot x^S + \mathbf{t}_i$.

IV. EXPERIMENTS

A. Datasets and Evaluation

We use the *in silico* dataset for both training and testing, while the *in vitro* dataset is used exclusively for testing. The same procedure (see §IV-B1) is applied to preprocess the input data for the baseline and the proposed methods (see §IV-B2).

1) *In silico phantom dataset*: Fig. 3 illustrates the generation process of the *in silico* dataset. We utilized CT scan volumes from the training dataset of the Medical Segmentation Decathlon [41] to generate liver models represented by 131 triangular meshes. These meshes were extracted using the marching cubes algorithm from the scikit-image Python library [42]. To enhance the quality of the mesh, we applied a Laplacian smoothing kernel and used vertex clustering with a voxel size of 2 mm from the Open3D Python library [43]. Finally, we used Tetgen [44] to generate volumetric mesh from the surface meshes. The liver models were split into 120 models for training and 11 models for testing. Each liver model was randomly scaled in the x, y, and z dimensions to augment

the data. The isotropic scale factors were uniformly generated from the range [0.5, 1]. This process generated 10 additional liver models for each original liver, resulting in 1,320 liver models for training and 121 liver models for testing.

For each liver model, we generated 10 deformations using the pipeline proposed in [18] via a finite element model and used its default parameters. Some simulated deformations feature rigid transformations instead of deformation when the randomly generated zero boundary condition is small. To eliminate rigid transformation, we further align the undeformed and deformed models with the SVD using the volumetric vertices as fiducial markers. After the alignment, the average root mean square error of the fiducial markers is 3.37 mm, with a maximum value of 11.38 mm, which is similar to the deformation range in Sparse Non-rigid Registration Challenge dataset [45].

For both training and testing datasets, we followed the previous works [12], [13], [31] to perform random cropping and rigid transformations on the deformed surface for each deformation. We calculate the visibility ratio as M/N . The visibility of the target point clouds was between 0.2 and 1.0. Regarding the rigid transformations, we sample rotations according to three Euler angle rotations in the range $[0, 2\pi]$ and translations in the range $[-100, 100]$ mm.

For the testing dataset, we generated five target point clouds for each deformation. Consequently, the testing dataset contained 121 source point clouds with 6,050 target point clouds.

The training dataset comprised 1,320 liver models with 13,200 deformed liver models after the deformation simulation. A specialized training strategy will be introduced later in IV-B to utilize the training dataset.

As illustrated in Fig. 3, the volumetric vertices are assumed to be fiducial markers for measuring registration accuracy.

2) *In vitro phantoms*: We used the phantom dataset constructed in [46] as a baseline to create another testing dataset to prove the generality of our proposed method. The phantom dataset contains four undeformed (source) and deformed (target) models with known embedded fiducial markers as validation points to compute the target registration errors. CT scans of both undeformed and deformed phantoms were acquired, and the ground truth surface mesh and fiducial landmarks were manually segmented from the CT scans. We generated 200 target point clouds from the complete target model surface, producing 800 testing samples.

3) *Evaluation*: A large number of evaluation metrics [12], [13], [23] exist to measure point cloud registration. However, these metrics rely on ground truth rigid transformations or one-to-one correspondence, which do not apply to our settings. Also, they do not provide insight into subsurface registration errors.

Here, we use the root mean square target registration error (RMS-TRE) to measure the final outcome of the registration methods on the above datasets. RMS-TRE offers an unbiased assessment of registration accuracy across the liver, including fiducial markers underneath the surface, and directly reflects the precision required when overlaying preoperative data onto

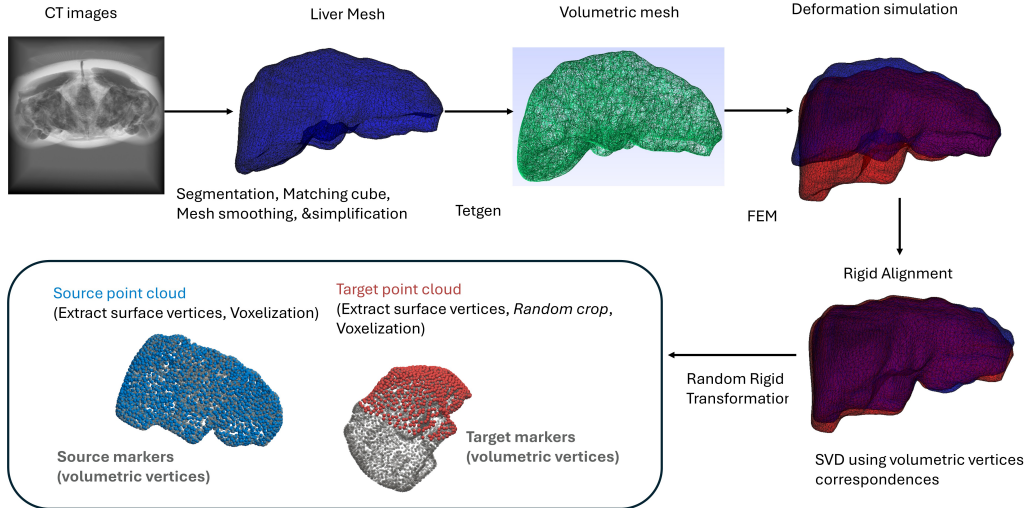


Fig. 3. Illustration of the *in silico* phantom generation process. Source and target point clouds/ meshes are shown in blue and red, respectively.

intraoperative data. It takes the form as:

$$\text{RMS-TRE} = \sqrt{\frac{\|\mathbf{Y} - \mathbf{W}(\mathbf{X})\|_2^2}{N_f}}, \quad (4)$$

where \mathbf{Y} and \mathbf{X} represent the locations of fiducial markers in the source and target, respectively, and N_f is the number of fiducial markers.

B. Implementations

1) *Preprocessing*: The preprocessing step is crucial as the point cloud feature learning models typically require a consistent point cloud density to extract features effectively. We begin by centering the source point cloud by subtracting its centroid, then scale it to fit within a unit sphere using the maximum distance from the origin. The target point cloud is processed similarly but scaled using the same factor as the source. Both point clouds are then voxelized with a voxel size of 0.04.

2) *Baselines*: We used the official implementations of the following methods: (1). Go-ICP [21], a traditional method that globally searches for a minimizing condition across SE(3). (2). RegTr [24], an end-to-end point cloud correspondence network that predicts a final set of correspondences directly rather than matching source and target features. (3). RoITr [26], a state-of-the-art method that utilizes a point-to-node strategy. (4). Leopard [13], another state-of-the-art method, excelling in rigid and non-rigid point cloud registration datasets. (5). LiverMatch [31], an available correspondence-based point cloud registration method specifically developed for liver surgery. RegTr [24], Leopard [13], and LiverMatch [31] leverage the power of KPConv [35] in their point cloud feature learning. The initial cell size in KPConv, which controls the downsampling rate, is set to 0.02 to enable gradual downsampling on our datasets. All the learning-based methods are implemented in PyTorch [47].

3) *Proposed module*: The only hyperparameter of the proposed module is the number of candidate patches, K , whose default value is set to 5. In §V-C, a sensitivity study is conducted to evaluate the impact of this hyperparameter on the downstream performance of the registration methods.

4) *Procrustes*: In addition to the baseline methods, we also include Procrustes, which uses SVD with ground truth fiducial markers to estimate the rigid registration. This method serves as a reference for deformation and potentially offers the best rigid registration that baseline methods can achieve.

5) *Statistical hypothesis test*: The Wilcoxon Rank Sum Test at a significance level of $\alpha = 0.05$ is used to assess whether integrating the proposed module with a baseline method significantly improves registration results compared to the original baseline performance.

6) *Training*: We used a special training strategy that fully exploits the *in silico* training dataset by dynamically selecting source and target point cloud pairs during training. Specifically, two source and target point clouds are randomly chosen from a liver and its deformations within the training dataset. Random cropping and rigid transformations are then applied to the target point cloud, as described in §IV-A1. Some baselines required either rigid transformation or correspondences between source and target point cloud. The required rigid transformation is obtained from Procrustes, and the correspondences are determined using nearest neighbor searching between the source and target point clouds within a radius of 0.04 after applying the Procrustes. For all methods, the maximum number of training epochs is set to 150, and the batch size is set to 1. Training is performed on an NVIDIA A100 GPU, with Leopard taking approximately three days to train, while other methods require about one day.

V. RESULTS

A. In Silico Phantom Validation

1) *Performance against Baselines*: We begin by evaluating the performance of the baseline methods under varying visi-

TABLE I
COMPARISON OF REGISTRATION ERRORS ON THE *In Silico* PHANTOM DATASET ACROSS DIFFERENT VISIBILITY RATIOS. THE AVERAGE RMS-TRE \pm STANDARD DEVIATION IS REPORTED IN MILLIMETERS.

Visibility ratio	[0.2, 0.3]	[0.3, 0.4]	[0.4, 0.5]	[0.5, 0.6]	[0.6, 0.7]	[0.7, 0.8]	[0.8, 0.9]	[0.9, 1]
Procrustes	3.19 \pm 1.93	3.44 \pm 2.16	3.41 \pm 2.13	3.42 \pm 2.19	3.38 \pm 2.17	3.41 \pm 2.17	3.39 \pm 2.01	3.31 \pm 2.08
GO-ICP [21]	66.96 \pm 17.2	66.98 \pm 19.52	56.4 \pm 23.52	55.61 \pm 25.41	44.83 \pm 29.27	33.56 \pm 29.94	19.9 \pm 24.21	5.42 \pm 2.65
RoITr [26]	20.21 \pm 25.12	10.77 \pm 12.71	7.24 \pm 8.13	5.6 \pm 6.05	4.61 \pm 3.57	4.19 \pm 2.61	3.91 \pm 2.36	3.75 \pm 2.46
RegTr [24]	84.27 \pm 29.46	69.89 \pm 30.16	59.66 \pm 30.45	48.08 \pm 30.11	33.53 \pm 24.36	20.24 \pm 11.89	12.05 \pm 4.16	5.82 \pm 2.41
LiverMatch [31]	12.85 \pm 13.87	8.09 \pm 6.88	6.65 \pm 5.15	5.65 \pm 3.98	4.79 \pm 2.82	4.24 \pm 2.45	3.84 \pm 2.09	3.56 \pm 2.07
LiverMatch [31] + proposed P2P	8.74 \pm 10.23	6.55 \pm 5.54	5.5 \pm 3.69	5.00 \pm 3.30	4.40 \pm 2.71	4.08 \pm 2.46	3.78 \pm 2.15	3.58 \pm 2.16
Lepard [13]	9.47 \pm 14.74	6.17 \pm 4.83	5.22 \pm 3.7	4.76 \pm 4.33	4.20 \pm 2.58	3.96 \pm 2.43	3.74 \pm 2.17	3.57 \pm 2.22
Lepard [13] + proposed P2P	6.73 \pm 5.96	5.63 \pm 3.72	4.96 \pm 3.28	4.60 \pm 2.93	4.22 \pm 2.68	4.00 \pm 2.50	3.78 \pm 2.22	3.59 \pm 2.25

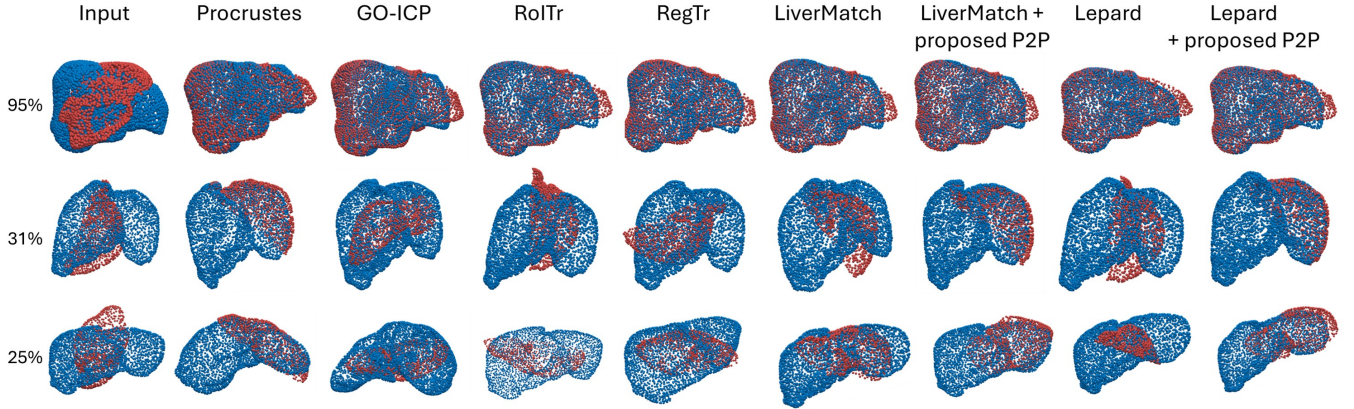


Fig. 4. Qualitative comparison of registration results on the *in silico* phantom dataset. The source and target point clouds are shown in blue and red, respectively.

TABLE II
REGISTRATION ERRORS ON THE *in silico* PHANTOM DATASET AT DIFFERENT NOISE LEVELS, WITHIN THE VISIBILITY RATIO RANGE [0.2, 0.3]. THE AVERAGE RMS-TRE \pm STANDARD DEVIATION IS REPORTED IN MILLIMETERS.

Noise level	0 mm	2 mm	4 mm
Procrustes	3.37 \pm 2.11	3.37 \pm 2.11	3.37 \pm 2.11
LiverMatch [31]	12.85 \pm 13.87	13.72 \pm 15.48	21.85 \pm 23.2
LiverMatch [31] + proposed P2P	8.74 \pm 10.23	9.19 \pm 9.48	14.58 \pm 18.11
Lepard [13]	9.47 \pm 14.74	10.07 \pm 15.28	14.7 \pm 21.02
Lepard [13] + proposed P2P	6.73 \pm 5.96	7.22 \pm 8.45	9.85 \pm 14.88

bility ratios, with the quantitative results summarized in Table I.

At higher visibility ratios (i.e., visibility $\in [0.9, 1.0]$), the baseline methods perform similarly to Procrustes, where rigid registration achieves the lowest errors, even in the presence of deformation. However, as the visibility ratio decreases, the performance of GO-ICP declines sharply, followed by RegTr, RoITr, LiverMatch, and Lepard. Among these, Lepard shows better robustness to changes in visibility, although its RMS-TRE still increases noticeably from 3.56 mm at visibility ratios $\in [0.9, 1.0]$ to 9.47 mm at visibility ratios $\in [0.2, 0.3]$

We then examine the results obtained by Lepard and LiverMatch with our proposed module, alongside those from RoITr quantitatively and qualitatively in Table I and Fig. 5, respectively. At the lowest visibility ratio range (i.e., visibility $\in [0.2, 0.3]$), the registration errors for Lepard decrease from 9.47 mm to 6.73 mm, and for LiverMatch, from 12.85 mm to 8.74 mm following the integration of our proposed module. These improvements are statistically significant.

2) *Sensitivity to Noise*: Given the promising results achieved by Lepard and LiverMatch with our proposed method, we further investigate their performance in the presence of noise and across groups with varying deformations in Table II. In our setting, noise is generated by sampling uniform random values from the range $[-0.5, 0.5]$, scaling them by the noise level, and applying them to the target point cloud. When the noise level increases from 2 to 4 mm, the performances of LiverMatch and Lepard decline by 59.25% and 43.92%, respectively. Our proposed method, on the other hand, helps both methods maintain lower RMS-TRE at these noise levels.

3) *Visual Assessment*: We further visualize the results in Fig. 4. In the first row, we show a case with a high visibility ratio as baseline, where all methods produce reasonable results. However, in the second and last rows, when the visibility ratio is low, all methods struggle to align the source to the target point cloud properly. After incorporating our proposed module, both LiverMatch and Lepard are able to achieve reasonable results.

B. In Vitro Phantom Validation

1) *Performance against Baselines*: We further compare the baseline methods with and without our proposed module using the phantom datasets. The results are reported in Table III. As seen, the *In Vitro* results align with the findings from the *In Silico* experiments. GO-ICP, RegTr, and RoITr are more sensitive to visibility variations compared to LiverMatch and Lepard. After applying our module, the RMS-TRE values for LiverMatch and Lepard are reduced from 20.54 mm to 14.97

TABLE III

COMPARISON OF REGISTRATION ERRORS ON THE *In Vitro* PHANTOM DATASET ACROSS DIFFERENT VISIBILITY RATIOS. THE AVERAGE RMS-TRE \pm STANDARD DEVIATION IS REPORTED IN MILLIMETERS.

Visibility ratio	[0.2, 0.3]	[0.3, 0.4]	[0.4, 0.5]	[0.5, 0.6]	[0.6, 0.7]	[0.7, 0.8]	[0.8, 0.9]	[0.9, 1]
Procrustes	3.66 \pm 1.69	3.67 \pm 1.78	3.91 \pm 1.74	3.58 \pm 1.8	3.43 \pm 1.68	3.62 \pm 1.7	3.77 \pm 1.6	3.65 \pm 1.91
GO-ICP [21]	87.15 \pm 25.91	82.58 \pm 25.45	75.34 \pm 25.53	72.2 \pm 30.03	61.89 \pm 30.91	47.04 \pm 36.66	21.16 \pm 26.16	9.31 \pm 19.08
RoITr [26]	33.8 \pm 24.06	17.03 \pm 17.2	12.67 \pm 14.43	8.34 \pm 9.33	5.7 \pm 3.69	4.66 \pm 2.21	4.39 \pm 1.8	4.1 \pm 2.09
RegTr [24]	66.25 \pm 16.15	55.91 \pm 19.19	45.02 \pm 20.19	37.39 \pm 21.67	29.74 \pm 20.48	16.15 \pm 13.07	8.76 \pm 2.66	5.16 \pm 1.8
LiverMatch [31]	20.54 \pm 22.33	12.46 \pm 12.87	8.26 \pm 5.34	6.69 \pm 4.29	5.26 \pm 3.16	4.66 \pm 2.58	4.18 \pm 1.7	3.85 \pm 1.85
LiverMatch [31] + proposed P2P	14.97 \pm 18.73	9.21 \pm 7.95	6.98 \pm 4.51	5.66 \pm 2.80	4.74 \pm 3.03	4.5 \pm 2.26	4.17 \pm 1.74	3.83 \pm 1.92
Lepard [13]	20.71 \pm 23.39	10.32 \pm 12.03	6.58 \pm 4.33	5.3 \pm 2.62	4.65 \pm 3.09	4.24 \pm 1.96	4.14 \pm 1.72	3.86 \pm 1.96
Lepard [13] + proposed P2P	12.45 \pm 15.72	8.43 \pm 9.64	6.07 \pm 3.12	5.08 \pm 2.58	4.45 \pm 2.38	4.26 \pm 2.01	4.19 \pm 1.78	3.91 \pm 2.02

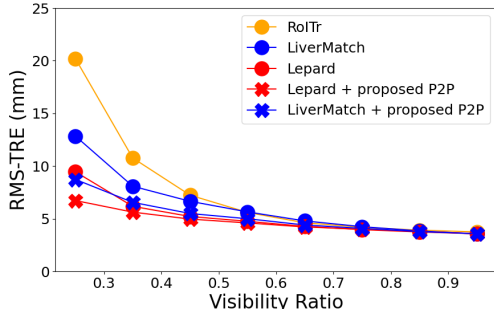


Fig. 5. Comparison of registration errors from the *in silico* phantom dataset, with the average RMS-TRE values plotted against different visibility ratios using the bin centers from Table I.

mm and from 20.71 mm to 12.45 mm, respectively. These improvements are statistically significant.

2) *Visual Assessment*: For both the *in silico* and *in vitro* datasets, the target point clouds are automatically cropped. Additionally, we present qualitative results using manually cropped surfaces from [46], as shown in Fig. 6. In these manually cropped cases, the proposed method still significantly improves the registration results compared to Lepard. Overall, we demonstrate that the versatility of our proposed module enables seamless plug-and-play integration to improve the robustness and reliability of deep learning methods for rigid point cloud registration.

C. Sensitivity and Ablation study

TABLE IV

ABLATION STUDY ON THE SELECTION METHOD AND CANDIDATE PROPOSAL, PERFORMED ON THE *in vitro* PHANTOM DATASET AT A VISIBILITY RANGE OF [0.2, 0.3], USING LEPARD AS THE BASELINE FOR THE PROPOSED MODULE. THE AVERAGE RMS-TRE \pm STANDARD DEVIATION IS REPORTED IN MILLIMETERS.

Selection rule	Inlier number	14.14 \pm 16.70
	Closest point distance (default)	12.45 \pm 15.72
Candidate proposal	w/o	14.91 \pm 19.06
	w/ (default)	12.45 \pm 15.72

We further conduct comprehensive sensitivity and ablation studies on the phantom dataset, incorporating the proposed module with Lepard to evaluate its effectiveness.

Candidate patch number. The only hyperparameter in the proposed module is the candidate patch number, K . We vary this hyperparameter and present the registration results in Fig. 7, which shows a clear trend of decreasing registration

error as the number of candidate patches increases. Statistical significance was observed between $K = 4$ and $K = 5$, but not between $K = 5$ and $K = 6$, suggesting that the default value of $K = 5$ provides an optimal balance between computational complexity and accuracy.

Selection role. We further compare our closest distance-based selection introduced in Eq. 3, with the inlier number-based selection in Eq. 2, where the parameter τ is set to 0.05. As shown in Table IV, our approach proves to be more effective, resulting in fewer errors below 2 mm.

Patch candidate proposal. We also investigate the contribution of the candidate proposal to our proposed module. As shown in Table IV, omitting the patch candidate proposal results in a significant decline in performance, with a drop of approximately 2.5 mm in registration accuracy.

Comparison with RANSAC. Following previous studies [24], [26], we further compare the proposed module with RANSAC, a typical robust estimator used in point cloud registration. As discussed in Section II-B, the robust estimators do not fit the end-to-end learning scheme and are not designed to handle the complete-to-partial ambiguity.

Using the correspondence-based RANSAC ICP implementation from Open3D [43], with the hyperparameter for maximum correspondence distance set to 0.05, we found that our proposed module consistently outperforms RANSAC, particularly in low-visibility scenarios. RANSAC slightly worsened registration results in the visibility range [0.4, 1), likely due to its random sampling nature. The average running time of the proposed module is 0.04 seconds, compared to 1.06 seconds for RANSAC.

VI. DISCUSSION

While learning-based point cloud registration methods are grounded in a solid foundation in natural benchmarks, they face a unique challenge from the complete-to-partial ambiguity when applied to liver surgery scenarios, where only a partial surface is visible during an intraoperative operation.

To alleviate this ambiguity, we propose a patches-to-partial feature matching module to bridge the gap between methods and their applications in liver surgery. Also, as a comprehensive benchmark is missing in this field, we construct a benchmark consisting of *in silico* and *in vitro* datasets.

We then evaluate representative correspondence-based methods on the constructed datasets. While these methods achieve comparable registration errors in high-visibility cases, their performance deteriorates as the visibility ratio decreases.

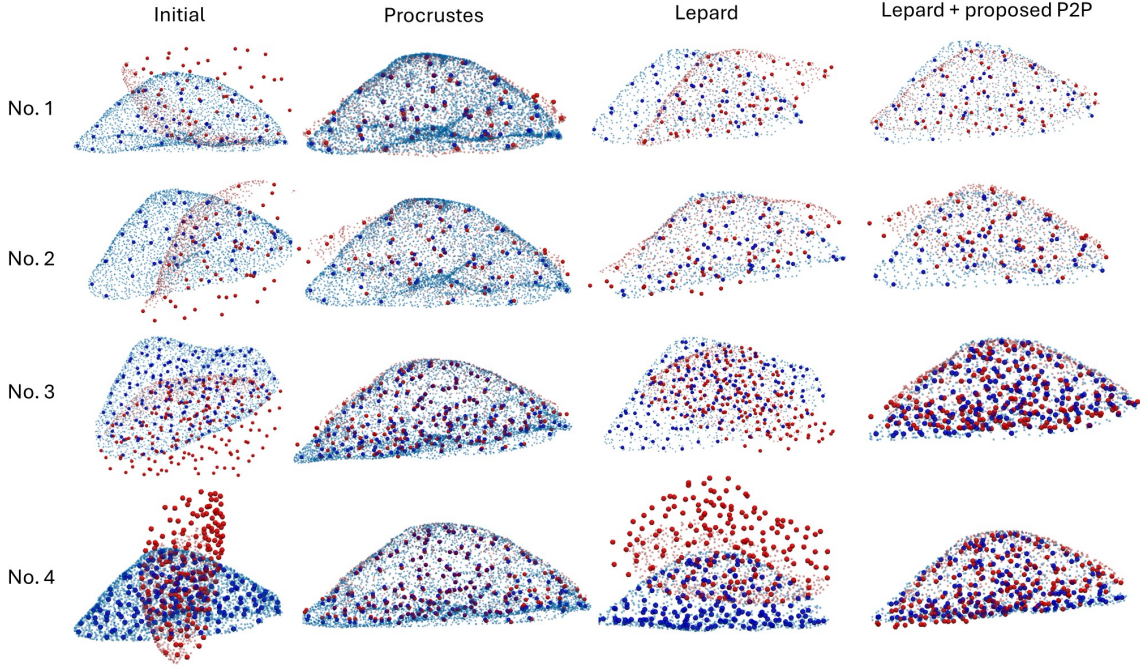


Fig. 6. Qualitative comparison of registration results on the *in vitro* phantom dataset. The source point cloud and its fiducial markers are shown in blue, while the target point cloud and its fiducial markers are shown in red, with fiducial markers displayed in larger sizes for visibility.

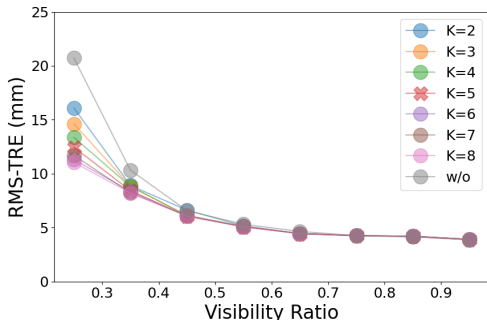


Fig. 7. Sensitivity study on cluster number K , performed on the *in vitro* phantom dataset at different visibility ratio, using Lepard as the baseline for the proposed module.

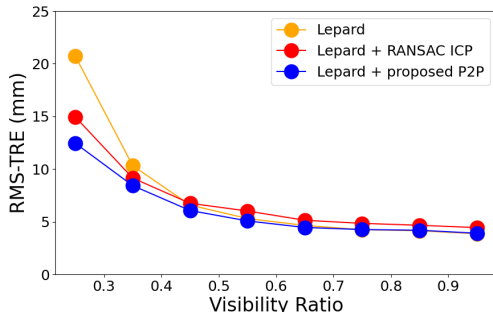


Fig. 8. Comparison of the proposed module with RANSAC ICP on the *in vitro* phantom dataset.

Among them, RegTr is particularly sensitive to reduced visibility, likely due to its unique design. RegTr directly predicts the displacements of source and target key points as correspondences, rather than matching features between the two point

clouds. This approach works well when the source and target point clouds are of similar scale, but in cases of complete-to-partial ambiguity, predicting key point displacements is less robust due to the lack of global context from the target point cloud. RoITr, a method based on the node-to-group strategy, also shows sensitivity to low-visibility cases. Its node-to-group strategy is not designed to handle complete-to-partial ambiguity but rather aims to find more correspondences through a coarse-to-fine search. In comparison with RegTr and RoITr, LiverMatch and Lepard are less sensitive to decreasing visibility ratios. Both methods employ a U-Net-like structure and match features between the source and target point clouds at the final output, indicating that this simple pipeline may be more versatile. Despite showing promising results from LiverMatch and Lepard, their performances are still not satisfying in low-visibility cases. In such instances, after applying our module, we observe significant improvements *w.r.t.* the registration performance (see Table I, III), having merits in:

i) Our proposed module alleviates the complete-to-partial ambiguity by converting it to patches-to-partial matching. Our module only has one hyperparameter, K , whose physical meaning controls the number of proposed patches. From the parameter-sensitivity study shown in Fig. 7, increasing K will improve the registration by expanding a fully parallelizable search space, and the default value $K = 5$ yields satisfactory results. In addition, we conducted an ablation study on our candidate proposal, and the closest point distance-based selection rule effectively contributes to the whole strategy.

ii) Our proposed module can be seamlessly integrated with several learning-based correspondence methods to handle complete-to-partial ambiguity. The proposed module is differentiable, fast, and parameter-free, as it only involves

feature resampling and matching and runs in parallel on the GPU. The proposed module contributes to advancing the robustness and reliability of fully automatic end-to-end point cloud registration.

Limitations. The registration results depend on the condition that the source and target point clouds have similar densities. This may not hold if a very sparse target point cloud is manually collected via optical trackers. However, point cloud resampling methods may alleviate this limitation.

Experiments conducted in this paper are based on our constructed *in silico* and *in vitro* datasets. While our experiments have promisingly established a solid foundation for real-world applications, in future work, we will seek possibilities to construct an *in vivo* dataset to validate the performance of correspondence-based methods further.

VII. CONCLUSION

We have constructed a benchmark using both *in silico* and *in vitro* datasets to evaluate state-of-the-art learning-based point cloud matching methods. Our analysis underscores the challenge of complete-to-partial ambiguity in scenarios with low visibility ratios, as typically occurs during liver surgery. In light of this view, we introduce a patches-to-partial strategy as a module that can be seamlessly integrated with learning-based point cloud correspondence methods.

We have demonstrated the effectiveness of this module in improving several methods, especially in low-visibility conditions. To summarize, the constructed benchmark and the proposed module lay a solid foundation for future studies of *in vivo* applications.

REFERENCES

- [1] J. S. Heiselman, W. R. Jarnagin, and M. I. Miga, "Intraoperative correction of liver deformation using sparse surface and vascular features via linearized iterative boundary reconstruction," *IEEE transactions on medical imaging*, vol. 39, no. 6, pp. 2223–2234, 2020.
- [2] J. N. Smit, K. F. Kuhlmann, B. R. Thomson, N. F. Kok, T. J. Ruers, and M. Fusaglia, "Ultrasound guidance in navigated liver surgery: toward deep-learning enhanced compensation of deformation and organ motion," *International journal of computer assisted radiology and surgery*, pp. 1–9, 2023.
- [3] I. Peterlík, H. Courtecuisse, R. Rohling, P. Abolmaesumi, C. Nguan, S. Cotin, and S. Salcudean, "Fast elastic registration of soft tissues under large deformations," *Medical image analysis*, vol. 45, pp. 24–40, 2018.
- [4] O. V. Ivashchenko, K. F. Kuhlmann, R. van Veen, B. Pouw, N. F. Kok, N. J. Hoetjes, J. N. Smit, E. G. Klompenhouwer, J. Nijkamp, and T. J. Ruers, "Cbct-based navigation system for open liver surgery: Accurate guidance toward mobile and deformable targets with a semi-rigid organ approximation and electromagnetic tracking of the liver," *Medical physics*, vol. 48, no. 5, pp. 2145–2159, 2021.
- [5] D. C. Rucker, Y. Wu, L. W. Clements, J. E. Ondrake, T. S. Pfeiffer, A. L. Simpson, W. R. Jarnagin, and M. I. Miga, "A mechanics-based nonrigid registration method for liver surgery using sparse intraoperative data," *IEEE transactions on medical imaging*, vol. 33, no. 1, pp. 147–158, 2013.
- [6] B. Koo, M. R. Robu, M. Allam, M. Pfeiffer, S. Thompson, K. Gurusamy, B. Davidson, S. Speidel, D. Hawkes, D. Stoyanov, *et al.*, "Automatic, global registration in laparoscopic liver surgery," *International Journal of Computer Assisted Radiology and Surgery*, pp. 1–10, 2022.
- [7] S. Suwelack, S. Röhl, S. Bodenstedt, D. Reichard, R. Dillmann, T. dos Santos, L. Maier-Hein, M. Wagner, J. Wünscher, H. Kennigott, *et al.*, "Physics-based shape matching for intraoperative image guidance," *Medical physics*, vol. 41, no. 11, p. 111901, 2014.
- [8] N. Golse, A. Petit, M. Lewin, E. Vibert, and S. Cotin, "Augmented reality during open liver surgery using a markerless non-rigid registration system," *Journal of Gastrointestinal Surgery*, vol. 25, pp. 662–671, 2021.
- [9] B. Acidi, M. Ghallab, S. Cotin, E. Vibert, and N. Golse, "Augmented reality in liver surgery, where we stand in 2023," *Journal of Visceral Surgery*, 2023.
- [10] A. Teatini, E. Pelanis, D. L. Aghayan, R. P. Kumar, R. Palomar, Å. A. Fretland, B. Edwin, and O. J. Elle, "The effect of intraoperative imaging on surgical navigation for laparoscopic liver resection surgery," *Scientific Reports*, vol. 9, no. 1, p. 18687, 2019.
- [11] A. Zeng, S. Song, M. Nießner, M. Fisher, J. Xiao, and T. Funkhouser, "3dmatch: Learning local geometric descriptors from rgb-d reconstructions," in *Proceedings of the IEEE conference on computer vision and pattern recognition*, pp. 1802–1811, 2017.
- [12] S. Huang, Z. Gojcic, M. Usvyatsov, A. Wieser, and K. Schindler, "Predator: Registration of 3d point clouds with low overlap," in *Proceedings of the IEEE/CVF Conference on computer vision and pattern recognition*, pp. 4267–4276, 2021.
- [13] Y. Li and T. Harada, "Lepard: Learning partial point cloud matching in rigid and deformable scenes," in *Proceedings of the IEEE/CVF conference on computer vision and pattern recognition*, pp. 5554–5564, 2022.
- [14] H. Yu, F. Li, M. Saleh, B. Busam, and S. Ilic, "Cofinet: Reliable coarse-to-fine correspondences for robust pointcloud registration," *Advances in Neural Information Processing Systems*, vol. 34, pp. 23872–23884, 2021.
- [15] Z. Wu, S. Song, A. Khosla, F. Yu, L. Zhang, X. Tang, and J. Xiao, "3d shapenets: A deep representation for volumetric shapes," in *Proceedings of the IEEE conference on computer vision and pattern recognition*, pp. 1912–1920, 2015.
- [16] C. R. Qi, H. Su, K. Mo, and L. J. Guibas, "Pointnet: Deep learning on point sets for 3d classification and segmentation," in *Proceedings of the IEEE conference on computer vision and pattern recognition*, pp. 652–660, 2017.
- [17] J. S. Heiselman, L. W. Clements, J. A. Collins, J. A. Weis, A. L. Simpson, S. K. Geevarghese, T. P. Kingham, W. R. Jarnagin, and M. I. Miga, "Characterization and correction of intraoperative soft tissue deformation in image-guided laparoscopic liver surgery," *Journal of Medical Imaging*, vol. 5, no. 2, pp. 021203–021203, 2018.
- [18] M. Pfeiffer, C. Riediger, S. Leger, J.-P. Kühn, D. Seppelt, R.-T. Hoffmann, J. Weitz, and S. Speidel, "Non-rigid volume to surface registration using a data-driven biomechanical model," in *International Conference on Medical Image Computing and Computer-Assisted Intervention*, pp. 724–734, Springer, 2020.
- [19] P. J. Besl and N. D. McKay, "Method for registration of 3-d shapes," in *Sensor fusion IV: control paradigms and data structures*, vol. 1611, pp. 586–606, Spie, 1992.
- [20] K. S. Arun, T. S. Huang, and S. D. Blostein, "Least-squares fitting of two 3-d point sets," *IEEE Transactions on pattern analysis and machine intelligence*, pp. 698–700, 1987.
- [21] J. Yang, H. Li, D. Campbell, and Y. Jia, "Go-icp: A globally optimal solution to 3d icp point-set registration," *IEEE transactions on pattern analysis and machine intelligence*, vol. 38, no. 11, pp. 2241–2254, 2015.
- [22] Y. Aoki, H. Goforth, R. A. Srivatsan, and S. Lucey, "Pointnetlk: Robust & efficient point cloud registration using pointnet," in *Proceedings of the IEEE/CVF conference on computer vision and pattern recognition*, pp. 7163–7172, 2019.
- [23] H. Xu, S. Liu, G. Wang, G. Liu, and B. Zeng, "Omnet: Learning overlapping mask for partial-to-partial point cloud registration," in *Proceedings of the IEEE/CVF International Conference on Computer Vision*, pp. 3132–3141, 2021.
- [24] Z. J. Yew and G. H. Lee, "Regtr: End-to-end point cloud correspondences with transformers," in *Proceedings of the IEEE/CVF conference on computer vision and pattern recognition*, pp. 6677–6686, 2022.
- [25] Z. Qin, H. Yu, C. Wang, Y. Guo, Y. Peng, and K. Xu, "Geometric transformer for fast and robust point cloud registration," in *Proceedings of the IEEE/CVF conference on computer vision and pattern recognition*, pp. 11143–11152, 2022.
- [26] H. Yu, Z. Qin, J. Hou, M. Saleh, D. Li, B. Busam, and S. Ilic, "Rotation-invariant transformer for point cloud matching," in *Proceedings of the IEEE/CVF conference on computer vision and pattern recognition*, pp. 5384–5393, 2023.
- [27] X. Zhang, J. Yang, S. Zhang, and Y. Zhang, "3d registration with maximal cliques," in *Proceedings of the IEEE/CVF Conference on Computer Vision and Pattern Recognition*, pp. 17745–17754, 2023.
- [28] T. R. dos Santos, A. Seitel, T. Kilgus, S. Suwelack, A.-L. Wekerle, H. Kennigott, S. Speidel, H.-P. Schlemmer, H.-P. Meinzer, T. Heimann, *et al.*, "Pose-independent surface matching for intra-operative soft-tissue marker-less registration," *Medical image analysis*, vol. 18, no. 7, pp. 1101–1114, 2014.

- [29] M. R. Robu, J. Ramalhinho, S. Thompson, K. Gurusamy, B. Davidson, D. Hawkes, D. Stoyanov, and M. J. Clarkson, "Global rigid registration of ct to video in laparoscopic liver surgery," *International Journal of Computer Assisted Radiology and Surgery*, vol. 13, no. 6, pp. 947–956, 2018.
- [30] P. Guan, H. Luo, J. Guo, Y. Zhang, and F. Jia, "Intraoperative laparoscopic liver surface registration with preoperative ct using mixing features and overlapping region masks," *International Journal of Computer Assisted Radiology and Surgery*, pp. 1–11, 2023.
- [31] Z. Yang, R. Simon, and C. A. Linte, "Learning feature descriptors for pre-and intra-operative point cloud matching for laparoscopic liver registration," *International Journal of Computer Assisted Radiology and Surgery*, pp. 1–8, 2023.
- [32] Y. Zhang, Y. Zou, and P. X. Liu, "Point cloud registration in laparoscopic liver surgery using keypoint correspondence registration network," *IEEE Transactions on Medical Imaging*, 2024.
- [33] R. Modrzejewski, T. Collins, B. Seeliger, A. Bartoli, A. Hostettler, and J. Marescaux, "An in vivo porcine dataset and evaluation methodology to measure soft-body laparoscopic liver registration accuracy with an extended algorithm that handles collisions," *International journal of computer assisted radiology and surgery*, vol. 14, no. 7, pp. 1237–1245, 2019.
- [34] C. R. Qi, L. Yi, H. Su, and L. J. Guibas, "Pointnet++: Deep hierarchical feature learning on point sets in a metric space," *Advances in neural information processing systems*, vol. 30, 2017.
- [35] H. Thomas, C. R. Qi, J.-E. Deschud, B. Marcotegui, F. Goulette, and L. J. Guibas, "Kpconv: Flexible and deformable convolution for point clouds," in *Proceedings of the IEEE/CVF international conference on computer vision*, pp. 6411–6420, 2019.
- [36] H. Zhao, L. Jiang, J. Jia, P. H. Torr, and V. Koltun, "Point transformer," in *Proceedings of the IEEE/CVF international conference on computer vision*, pp. 16259–16268, 2021.
- [37] R. Sinkhorn and P. Knopp, "Concerning nonnegative matrices and doubly stochastic matrices," *Pacific Journal of Mathematics*, vol. 21, no. 2, pp. 343–348, 1967.
- [38] I. Rocco, M. Cimpoi, R. Arandjelović, A. Torii, T. Pajdla, and J. Sivic, "Neighbourhood consensus networks," *Advances in neural information processing systems*, vol. 31, 2018.
- [39] K. S. Arun, T. S. Huang, and S. D. Blostein, "Least-squares fitting of two 3-d point sets," *IEEE Transactions on pattern analysis and machine intelligence*, no. 5, pp. 698–700, 1987.
- [40] J. Sun, Z. Shen, Y. Wang, H. Bao, and X. Zhou, "Loftr: Detector-free local feature matching with transformers," in *Proceedings of the IEEE/CVF conference on computer vision and pattern recognition*, pp. 8922–8931, 2021.
- [41] M. Antonelli, A. Reinke, S. Bakas, K. Farahani, A. Kopp-Schneider, B. A. Landman, G. Litjens, B. Menze, O. Ronneberger, R. M. Summers, et al., "The medical segmentation decathlon," *Nature communications*, vol. 13, no. 1, p. 4128, 2022.
- [42] S. Van der Walt, J. L. Schönberger, J. Nunez-Iglesias, F. Boulogne, J. D. Warner, N. Yager, E. Goullart, and T. Yu, "scikit-image: image processing in python," *PeerJ*, vol. 2, p. e453, 2014.
- [43] Q.-Y. Zhou, J. Park, and V. Koltun, "Open3D: A modern library for 3D data processing," *arXiv:1801.09847*, 2018.
- [44] S. Hang, "Tetgen, a delaunay-based quality tetrahedral mesh generator," *ACM Trans. Math. Softw.*, vol. 41, no. 2, p. 11, 2015.
- [45] J. S. Heiselman, J. A. Collins, M. J. Ringel, T. Peter Kingham, W. R. Jarnagin, and M. I. Miga, "The image-to-physical liver registration sparse data challenge: comparison of state-of-the-art using a common dataset," *Journal of Medical Imaging*, vol. 11, no. 1, pp. 015001–015001, 2024.
- [46] Z. Yang, R. Simon, K. Merrell, and C. A. Linte, "Boundary constraint-free biomechanical model-based surface matching for intraoperative liver deformation correction," *IEEE Transactions on Medical Imaging*, 2024.
- [47] A. Paszke, S. Gross, F. Massa, A. Lerer, J. Bradbury, G. Chanan, T. Killeen, Z. Lin, N. Gimelshein, L. Antiga, A. Desmaison, A. Kopf, E. Yang, Z. DeVito, M. Raison, A. Tejani, S. Chilamkurthy, B. Steiner, L. Fang, J. Bai, and S. Chintala, "Pytorch: An imperative style, high-performance deep learning library," *Advances in Neural Information Processing Systems*, 2019.